Figure 4 Dependence of output energy on the input pump energy near threshold for 1-mm-long slab-waveguide (right inset) and double-heterostructure (left inset) laser devices whose structures are illustrated. Solid lines are fits to the data; η is the laser slope efficiency.

practical application of electrical injection lasers based on these compounds.

The dependence of output energy on the pump energy for the slab and double-heterostructure devices, shown in Fig. 4, clearly indicates a threshold. To reduce mirror losses, long ($\sim$1-mm) laser cavities were used to obtain the differential quantum efficiency (η) above threshold. We find that $\eta = 30\%$ for a slab device, and $\eta = 70\%$ for a double-heterostructure laser. The significantly higher differential efficiency and lower threshold of the double-heterostructure device as compared to the slab structure provides clear evidence for optical confinement in the Alq_3/DCM layer as compared to the cladding, as required for low-threshold electrically pumped injection lasers.

The thickness of the active layer in electrically pumped double heterostructures is ultimately limited by the hole diffusion length in Alq_3/DCM film, which is $\sim$100 Å (ref. 6). To assess the prospects for lasing in such structures, we also fabricated a double-heterostructure device with a 50-Å-thick active layer, which had a threshold pump energy density of 1 μJ cm^{-2} corresponding to a carrier density of 1.5×10^{12} cm^{-2}. Assuming a spontaneous radiative lifetime of 10 ns for Alq_3 and DCM[15], and assuming that only 25% of the electrically injected carriers form singlet excitons[16], we estimate a threshold current density for pulsed electrical injection of $\sim$100 A cm^{-2}, which is achievable under low-duty-cycle pulsed excitation in electrically pumped organic light-emitting devices based on Alq_3. One obstacle which might prevent the realization of small-molecule-based organic lasers is non-radiative exciton recombination (or quenching) previously observed at high carrier densities. For example, bimolecular reactions in Alq_3 films[15] have been found to decrease the photoluminescent quantum efficiency significantly at incident intensities above 10^{14} photons cm^{-2}. However, the lasing threshold in Alq_3/DCM films discussed here is at pump intensities of only 10^{12} photons cm^{-2}, leaving ample room for increased pump intensities without a decrease in efficiency.

We have shown low-threshold (1 μJ cm^{-2}), high-efficiency (70%), narrow-linewidth ($<$1 Å), high-output-power ($>$50 W) lasing at $\lambda = 645$ nm in vacuum-deposited organic semiconductor thin films. The pump thresholds for organic double heterostructures are estimated at 100 A cm^{-2} for an electrically pumped laser. The ease of processing, low threshold, high stability and other characteristics of vacuum deposited materials should open the way towards realizing a new generation of electrically pumped solid-state lasers based on organic thin films. □

1. Soffer, B. H. & McFarland, B. B. Continuously tunable, narrow-band organic dye lasers. *Appl. Phys. Lett.* **10**, 266–267 (1967).
2. Kogelnik, H. & Shank, C. V. Stimulated emission in a periodic structure. *Appl. Phys. Lett.* **18**, 152–154 (1971).
3. Karl, N. Laser emission from an organic molecular crystal. *Phys. Status Solidi* **13**, 651–655 (1972).
4. Hermes, R. E., Allik, T. H., Chandra, S. & Hutchinson, J. A. High-efficiency pyrromethene doped solid-state dye lasers. *Appl. Phys. Lett.* **63**, 877–879 (1993).
5. Burroughes, J. H. *et al.* Light-emitting diodes based on conjugated polymers. *Nature* **347**, 539–541 (1990).
6. Tang, C. W., VanSlyke, S. A. & Chen, C. H. Electroluminescence of doped organic thin films. *J. Appl. Phys.* **65**, 3610–3615 (1989).
7. Hide, F. *et al.* Semiconducting polymers: a new class of solid-state laser materials. *Science* **273**, 1833–1836 (1996).
8. Hide, F., Schwartz, B. J., Diaz-Garcia, M. A. & Heeger, A. J. Laser emission from solutions and films containing semiconducting polymer and titanium dioxide nanocrystals. *Chem. Phys. Lett.* **256**, 424–430 (1996).
9. Tessler, N., Denton, D. J. & Friend, R. H. Lasing from conjugated polymer microcavities. *Nature* **382**, 695–697 (1996).
10. Kozlov, V. G., Burrows, P. E. & Forrest, S. R. in *Conf. on Lasers and Electro-optics (CLEO '97)* CPD-18 (Opt. Soc. Am., Baltimore, MD, 1997).
11. Garbuzov, D. Z., Bulović, V., Burrows, P. E. & Forrest, S. R. Photoluminescence efficiency and absorption of aluminum-tris-quinolate (Alq_3) thin films. *Chem. Phys. Lett.* **249**, 433–437 (1996).
12. Pope, M. & Swenberg, C. E. *Electronic Processes in Organic Crystals* (Clarendon, Oxford, 1982).
13. Schafer, F. P. *Dye Lasers* (Springer, Berlin, 1977).
14. Coldren, L. A. & Corzine, S. W. *Diode Lasers and Photonic Integrated Circuits* (Wiley, New York, 1995).
15. Sokolik, I., Priestly, R., Walser, A. D., Dorsinville, R. & Tang, C. W. Bimolecular reactions of singlet excitons in tris(8-hydroxyquinoline) aluminum. *Appl. Phys. Lett.* **69**, 4168–4170 (1996).
16. Brown, A. R. *et al.* Poly(p-phenylenevinylene) light-emitting didoes: enhanced electroluminescent efficiency through carrier confinement. *Appl. Phys. Lett.* **61**, 2793–2795 (1992).

Continuous formation of supported cubic and hexagonal mesoporous films by sol–gel dip-coating

Yunfeng Lu[*], **Rahul Ganguli**[*], **Celeste A. Drewien**[*], **Mark T. Anderson**[*], **C. Jeffrey Brinker**[*], **Weilang Gong**[†], **Yongxing Guo**[†], **Hermes Soyez**[‡], **Bruce Dunn**[‡], **Michael H. Huang**[§] **& Jeffrey I. Zink**[§]

[*] *Sandia National Laboratories and The University of New Mexico/NSF Center for Micro-Engineered Materials, The Advanced Materials Laboratory, 1001 University Blvd SE, Albuquerque, New Mexico 87106, USA*
[†] *Department of Earth and Planetary Sciences, The Univeristy of New Mexico, Albuquerque, New Mexico 87106, USA*
Departments of [‡] *Materials Science and* [§] *Chemistry, University of California, Los Angeles, California 90095-1595, USA*

Thin films of surfactant-templated mesoporous materials[1,2] could find applications in membrane-based separations, selective catalysis and sensors. Above the critical micelle concentration of a bulk silica–surfactant solution, films of mesophases with hexagonally packed one-dimensional channels can be formed at solid–liquid and liquid–vapour interfaces[3–5]. But this process is slow and the supported films[3,5] are granular and with the pore channels oriented parallel to the substrate surface, so that transport across the films is not facilitated by the pores. Ogawa[6,7] has reported a rapid spin-coating procedure for making transparent mesoporous films, but their formation mechanism, microstructure and pore accessibility have not been elucidated. Here we report a sol–gel-based dip-coating method for the rapid synthesis of continuous mesoporous thin films on a solid substrate. The influence of the substrate generates film mesostructures that have no bulk counterparts, such as composites with incipient liquid-crystalline order of the surfactant–silica phase. We are also able to form mesoporous films of the cubic phase, in which the pores are connected in a three-dimensional network that guarantees their accessibility from the film surface. We demonstrate and quantify this accessibility using a surface-acoustic-wave nitrogen-adsorption

technique. **We use fluorescence depolarization to monitor the evolution of the mesophase *in situ*, and see a progression through a sequence of lamellar to cubic to hexagonal structures that has not previously been reported.**

Continuous films with accessible porosity are frequently cited as a promising application of mesoporous materials[3–7]. It has been shown[3–5] that by exceeding the critical micelle concentration, c_{mc} of a bulk silica-surfactant solution, hexagonal liquid crystalline mesophases with one-dimensional pore channels (1-dH) form at solid–liquid and liquid–vapour interfaces by interfacial self-assembly[8]. However, this process is slow and supported films are granular[3,5], with an unfavourable orientation of the pore channels parallel to the substrate surface[3,5]. Ogawa[6,7] has reported a rapid spin-coating procedure that results in transparent films, but the film-formation mechanism and microstructure have not yet been elucidated. No previous studies have demonstrated accessibility of the mesophase porosity of a supported film.

Our process begins with a homogeneous solution with an initial surfactant concentration $c_o \ll c_{mc}$. We rely on surfactant enrichment by solvent evaporation to exceed c_{mc} and therefore develop mesophases only during the last few seconds of film deposition (Fig. 1b). By varying c_o, we have access to a continuous range of silica/surfactant/solvent composition space, enabling us selectively to tailor the film morphology established at the drying line (Fig. 1b).

Precursor solutions were prepared by addition of cationic surfactant ($CTAB : CH_3(CH_2)_{15}N^+(CH_3)_3Br^-$) to polymeric silica sols made by a two-step process (A2**)[9], designed to minimize the siloxane condensation rate[10], promoting facile silica-surfactant co-assembly during film deposition. First, TEOS ($Si(OC_2H_5)_4$), ethanol water and HCl (mole ratios: $1 : 3 : 8 : 5 \times 10^{-5}$) were refluxed at 60 °C for 90 min. Second, water and HCl were added, increasing the concentration of HCl ([HCl]) to 7.34 mM. After stirring at 25 °C for
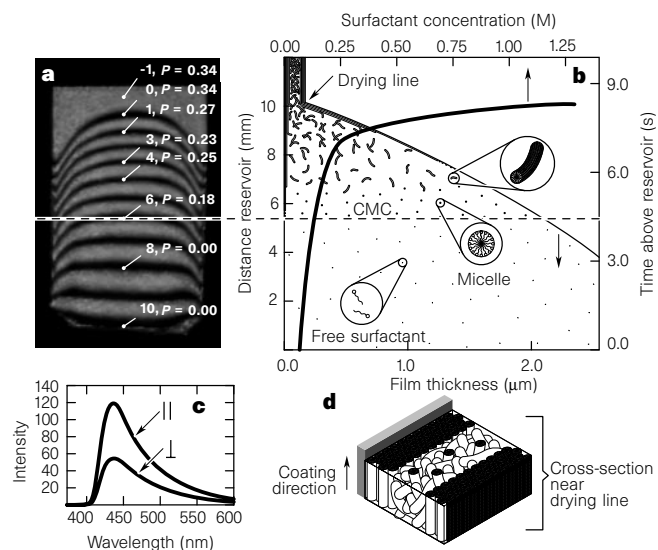
15 min, the sols were aged at 50 °C for 15 min and diluted 1 : 3 with ethanol. Finally, CTAB was added in quantities corresponding to concentrations in the range 0.03–0.11 M (1.5–5.0 wt%). The final reactant mole ratios were: $1\,TEOS : 22\,C_2H_5OH : 5\,H_2O : 0.004\,HCl : 0.054$–$0.18\,CTAB$.

Films were deposited on (100)-silicon by dip-coating at 7.6 cm min^{-1} (Fig. 1). During dip-coating[11], the entrained solution experiences preferential evaporation of ethanol[12], progressively enriching the concentrations of water, HCl, and the non-volatile constituents silica and surfactant. After several seconds, the film profile (thickness versus vertical position above the sol reservoir surface) becomes steady in the laboratory frame[11,12]. Figure 1a shows an interference image of a steady-state film acquired during dip-coating; Fig. 1b shows the corresponding film thickness and surfactant concentration profiles. The surfactant concentration increases by over an order of magnitude, whereas the surfactant/silica ratio remains constant.

Spatially resolved fluorescence-depolarization experiments[13] using a hydrophobic dye (2,6-TNS) entrained in the coating solution were performed in order to identify micelle formation *in situ* during film deposition (Fig. 1a, c). In the coating solution ($c_0 = 0.06$ M) and within the first ~5 mm above the reservoir surface, the degree of polarization, P, was zero indicating that the probe was freely rotating[13]. At fringe 6, which we identify as c_{mc}, P abruptly increases to 0.18 owing to incorporation of the probe in the hydrophobic micellar interior. Beyond c_{mc}, P continues to increase. In contrast, fluorescence depolarization of films prepared without CTAB gave $P \approx 0$ below the drying line and a finite P appeared only above the drying line. These results show that silica/surfactant micellar structures form only on the substrate by virtue of evaporation-induced surfactant enrichment.

Figure 2a shows X-ray diffraction patterns of supported, as-deposited films prepared with c_o in the range 0.06–0.11 M; Fig. 2b

Figure 1 a, Optical interference image of the steady-state film, prepared with initial surfactant concentration $c_o = 0.06$ M during dip-coating at 7.6 cm min^{-1}. The image was acquired using a HeNe laser ($\lambda = 632.8$ nm) and beam expander. Each fringe represents a change in the optical thickness of $\lambda/2(n^2 - \sin^2\theta)^{1/2}$, where n is the refractive index of the depositing sol and θ is the angle of incidence. Superimposed on the interference images are the values of P determined *in situ* as a function of fringe position above the sol reservoir (**c**). Fringes are numbered from 0 at the drying line to 10 near the reservoir surface (position −1 is located in the solidified film about one fringe spacing above the drying line). **b**, Steady-state film cross-section, corresponding to the interference image (**a**), with vertical axes representing distance above the sol reservoir surface and the corresponding time required for the substrate to move that distance. The film-thickness profile was calculated from the interference image assuming a linear refractive index gradient from 1.25 at the liquid meniscus to 1.35 at the drying line. The surfactant concentration was calculated from the thickness profile assuming no surfactant volatility; c_{mc} was established from the fluorescence depolarization experiments described in **a** and **c**. Although the surfactant concentration increases with position/time above the reservoir surface, the surfactant/silica ratio remains fixed. **c**, Fluorescence spectra of 2-*p*-toluidinyl napthalene-6-sulphonate (2,-6,TNS) acquired at fringe position −1. The probe molecule was introduced at an initial concentration of 10^{-4} M and excited at 351 nm with an argon ion laser polarized parallel to the film drawing direction. The beam was focused on a given fringe to a diameter of ~50 μm. Emitted light was analysed with a calcite Glan–Thompson polarizer oriented parallel (pl) or perpendicular (pp) to the incident light. The degree of polarization P was determined from the measured intensities I_{pl} and I_{pp} at 440 nm using the standard relation: $P = (I_{pl} - I_{pp})/(I_{pl} + I_{pp})$. P suddenly increases from 0 to 0.18 at fringe 6 owing to incorporation of the hydrophobic dye into the micellar interior, as verified by control solution experiments of CTAB in ethanol/water mixtures. **d**, Cross-section of an ordered region of the film near the drying line, depicting formation of interfacial regions of liquid crystalline order. 1-dH regions grow from the substrate–film and air–film interfaces towards the film interior. The proposed forma-

tion mechanism involves cooperative assembly of silica-surfactant micellar species with supramolecular surfactant 'templates', for example, cylindrical micelles or hemimicelles, that self-assemble at the substrate–liquid[3,5] and liquid–air interfaces[4] at an earlier stage of the deposition process (at or below c_{mc}; refs 3–5, 8). The interior region shows a disordered worm-like micellar structure[15]. Silica completely encases the surfactant assemblies, so that upon surfactant calcination a unimodal pore size is obtained. (Complementary *in situ* AFM experiments performed at the silicon(oxide)–liquid interface using the sol prepared with $c_o = 0.06$ M (S. Singh, unpublished results) showed the development of an interfacial structure with approximate thickness 0.15 nm over a period of 1 hour, confirming that film growth occurs almost exclusively during dip-coating.)
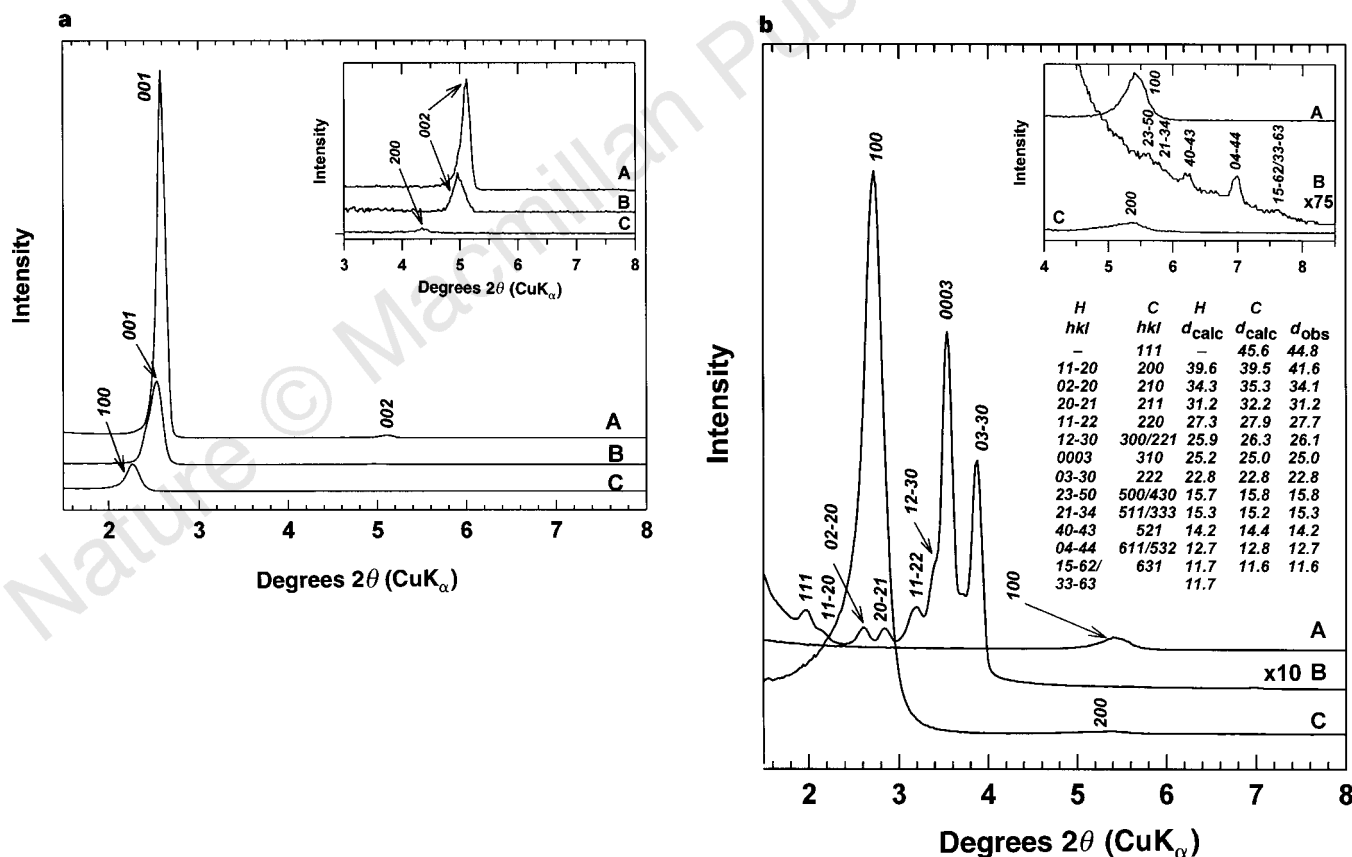
shows the corresponding patterns after calcination at 400 °C in oxygen. For the films prepared with $c_o = 0.06$ M, the X-ray diffraction is consistent with a 1-dH mesophase with pore channels oriented parallel to the substrate surface[3]. X-ray diffraction patterns of the uncalcined films prepared with $c_o = 0.10$ M and 0.11 M are consistent with an oriented lamellar liquid crystalline mesophase with basal spacing $c = 34.5$ Å (ref. 14). Upon calcination, the film prepared with $c_o = 0.11$ M collapses to form a substantially amorphous film, whereas the film prepared with $c_o = 0.10$ M transforms to a new mesostructure comprising both cubic and three-dimensional hexagonal (3-dH) liquid crystalline order. The (111)-peak in Fig. 2b, trace B, unambiguously establishes the cubic phase. The remaining peaks may be indexed on a primitive cubic cell with lattice constant $a = 78.9(12)$ Å or a related 3-dH cell with lattice constants $a = 79.1(5)$ Å and $c = 75.5(6)$ Å.

Figure 3a, b shows cross-sectional transmission electron micrographs (TEM) of calcined films. The film prepared with $c_o = 0.06$ M exhibits incipient 1-dH order adjacent to the air–film and film–substrate interfaces and a disordered interior region[15] with textural dimensions commensurate with the periodic interfacial structures. By comparison, the film prepared with $c_o = 0.10$ M exhibits a uniform silica mesophase characterized by a diamond-shaped lattice unique to the 3-dH hexagonal mesophase. Representative plan-view images are shown in Fig. 3c, d and 4c. The incipient 1-dH film is composed of swirling patterns of organized tubules[5] separated by disordered regions similar to the film interior. Swirling is consistent with the low bending energy of the tubules[5] and the inability of the liquid–vapour interface to impose long-range order on the tubule assembly process. In contrast, the cubic 3-dH film has extensive regions of three-dimensional ordering (image acquired through complete film thickness), with seamless transitions between ordered 'domains'.

To avoid any effects due to constrained one-dimensional shrinkage of the film normal to the substrate direction during calcination[3], film fragments were detached from the substrate before heating. No structures unique to the hexagonal phase have been observed in detached fragments. The TEM of a detached fragment (Fig. 4a) shows a square periodic lattice with spacing 79 Å, consistent with the (100)-orientation of the primitive cubic phase; Fig. 4b shows a simulated image with $a = 79$ Å.

We explain the formation of incipient 1-dH films as follows (Fig. 1b, d). Beginning with a homogeneous solution ($c_o \ll c_{mc}$), preferential ethanol evaporation enriches the depositing film in silica, surfactant and water, causing c to exceed c_{mc} at a CTAB

H hkl	C hkl	H d_{calc}	C d_{calc}	d_{obs}
–	111	–	45.6	44.8
11-20	200	39.6	39.5	41.6
02-20	210	34.3	35.3	34.1
20-21	211	31.2	32.2	31.2
11-22	220	27.3	27.9	27.7
12-30	300/221	25.9	26.3	26.1
0003	310	25.2	25.0	25.0
03-30	222	22.8	22.8	22.8
23-50	500/430	15.7	15.8	15.8
21-34	511/333	15.3	15.2	15.3
40-43	521	14.2	14.4	14.2
04-44	611/532	12.7	12.8	12.7
15-62/ 33-63	631	11.7 11.7	11.6	11.6

Figure 2 a, X-ray diffraction spectra (A–C) recorded on a Siemens D500 diffractometer using Ni-filtered CuKα radiation with $\lambda = 1.5418$ Å in θ–2θ scan mode for uncalcined silica/surfactant mesophases prepared with A, $c_o = 0.11$ M (5.0 wt% CTAB); B, $c_o = 0.10$ M (4.2 wt% CTAB); and C, $c_o = 0.06$ M (2.5 wt% CTAB). Inset: region where 2θ is 2.5–10°, with an intensity scale expanded 115 times, shows that all three spectra contain second-order reflections at $d = 1/2 d_{primary}$. **b**, XRD patterns of samples in **a** after calcination at 400 °C (heating rate of 1 °C min^{-1}). (Inset: region where 2θ is 3.5–10°, with an intensity scale expanded 15 times). Trace A (see **a**) is consistent with a lamellar liquid crystalline mesophase (L) with basal spacing $c = 34.5$ Å. The L mesophase collapses upon calcination (this panel), leaving only a tiny residual peak (0.5% of the intensity of the (001) peak of the uncalcined film) indicative of a small fraction of a non-collapsed, porous phase with $d \approx 16$ Å. Trace B (see **a**) resembles the L meso-phase of trace A, but upon calcination, the L film transforms to a new meso-structure composed of primitive cubic and 3-d hexagonal (3-dH) mesophases (this panel). (Apart from the (111) reflection, the peaks in trace B are indexed according to the 3-dH mesophase; the corresponding cubic indices (C) are shown in the table in the figure.) The cubic mesophase is characterized by $a = 78.9(12)$ Å, and the 3-dH mesophase by $a = 79.1(5)$ Å and $c = 75.6(6)$ Å. Note basal (0003) and prismatic (03-30) or cubic (222) preferred orientation of the C/3-dH film. Also the (111) peak is not indexable on the 3-dH unit cell, providing unique evidence for the cubic mesophase. Trace C is indicative of a 1-dH mesophase with a unit cell constant $a = 45.8$ Å (uncalcined) and $a = 37.8$ Å (calcined), in which the axes of the pore channels are oriented parallel to the substrate surface (note the absence of mixed reflections (110) and (210))[3].

concentration of ~ 0.1 M. Beyond c_{mc}, incipient liquid-crystalline domains 'grow' from both interfaces towards the centre (with an attendant increase in P) by co-assembly of silica-surfactant micellar species with the preorganized solid–liquid[3,5,16] and liquid–vapour interfacial regions[4]. Solidification at the drying line establishes a structure composed of disordered cylindrical micelles[15] sandwiched between ordered regions of hexagonal mesophases.

With increasing c_o (but still below c_{mc}), we observe incipient cubic (R.G., unpublished results) and lamellar mesophases that are consistent with a progressive evolution of the structure in response to surfactant enrichment. For $c_o \geqslant 0.10$ M, we believe homogeneous lamellar films (Fig. 4d) are nucleated by interfacially organized surfactant bilayers[16], observed using atomic force microscopy (AFM) for 0.11 M CTAB sols equilibrated with (100)-silicon (S. Singh, unpublished results). We suggest that cubic 3-dH films form by a lamellar → cubic → hexagonal pathway driven by continuing condensation of the siloxane framework as proposed[17] to explain lamellar to hexagonal transformations[18] in bulk silica mesophases. Although unreported for inorganic mesophases, lamellar to cubic transformations are common in CTAB[14] and

Figure 3 Cross-sectional TEM images (recorded with the silicon substrate oriented along the [110] zone axis) of: **a**, a calcined incipient 1-dH film, the same film used to obtain trace C in Fig. 2b. Periodic ordered regions (with different thicknesses) are observed at both the substrate–film and film–vapour (glue) interfaces mainly as stripes that transform into 'brick-like' features[3] for those domains with channel axes oriented approximately normal to the sectioning direction. Brick-like structures presumably result from constrained one-dimensional shrinkage of the films upon calcination[3]. **b**, the cubic 3-dH film prepared with $c_o = 0.10$ M, corresponding to trace B in Fig. 2b. The film is substantially ordered throughout its thickness. Electron diffraction and simulation uniquely identify this structure as the [$\bar{1}\bar{1}23$]-zone direction of the 3-dimensional hexagonal mesophase. Note the observed $68 \pm 2°$ angle between the ($10\bar{1}0$) and ($01\bar{1}1$) reflections. The calculated angle is 68.3°. This image cannot be accounted for by a 78.9-Å cubic cell. **c**, Plan-view image corresponding to the film–vapour interface for the same sample, as in **a** (recorded under identical conditions but with silicon substrate oriented along the [001] zone axis). The swirling patterns of tubule bundles show no preferred orientation and are similar in appearance to those observed by Aksay et al.[5] for silica-surfactant films grown at the silica–water interface. Interfaces between the swirls appear disordered but exhibit textural features comparable in dimension to the periodically ordered domains with no apparent gaps. **d**, Plan-view of cubic 3d-H film imaged through the complete film thickness and a thin layer of the underlying silicon substrate (note bend contours), showing seamless transition at a bend contour consistent with a continuous cubic 3-dH film. **e**, Scanning electron micrograph image of the incipient HLC film surface showing absence of granularity on macroscopic scales. (TEM samples were prepared by conventional sectioning techniques comprising grinding and polishing, followed by dimpling, and ion milling until electron-transparent.)
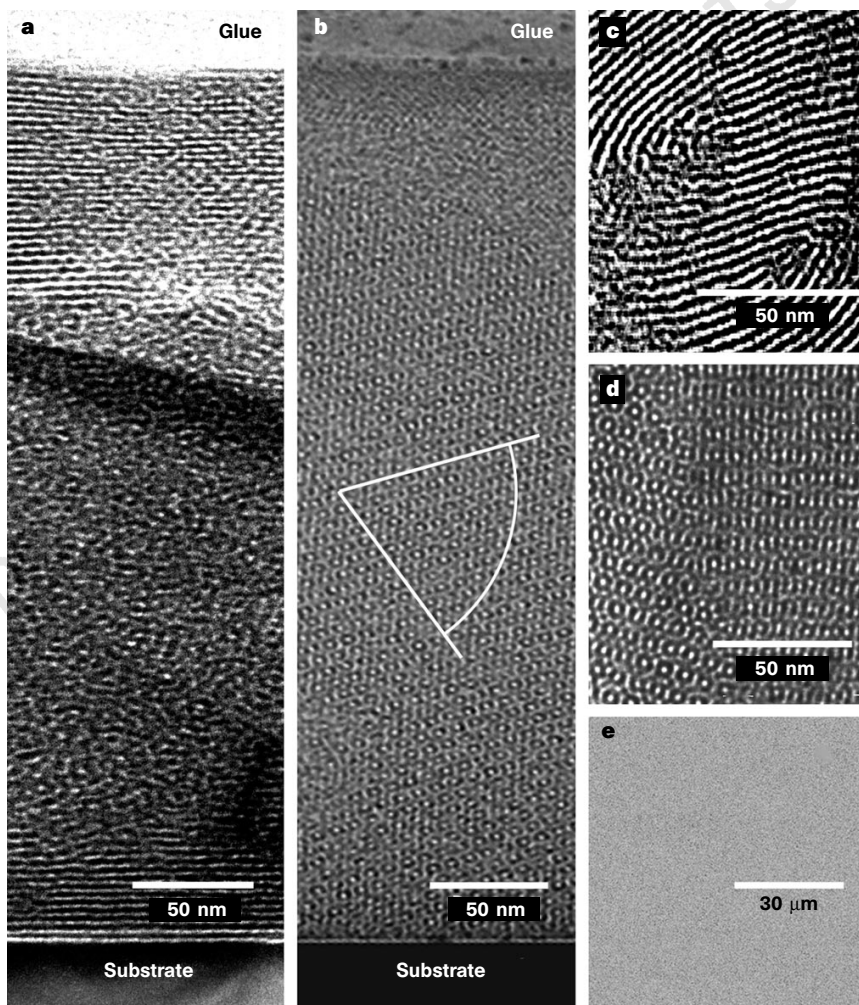
Figure 4 a, TEM image of the [100]-zone of a calcined film fragment prepared with $c_o = 0.10$ M and detached from the substrate before heating. The image shows the orthogonal arrangement of pores, with a pore-to-pore distance of ~ 79 Å, consistent with a cubic lattice. **b**, Simulated image of the [100]-oriented cubic mesophase, showing approximately the same phase contrast as the actual image. **c**, Plan-view of cubic 3d-H film imaged through the film and silicon substrate (not bend contours), showing a large region of [01-10] orientation. Inset: selected area defraction pattern of the [01-10] zone axis. Note this image and the selected area diffraction pattern are also consistent with the [210]-cubic orientation. **d**, Layered lamellar structure of the film prepared with $c_o = 0.10$ M before transformation to the cubic phase.
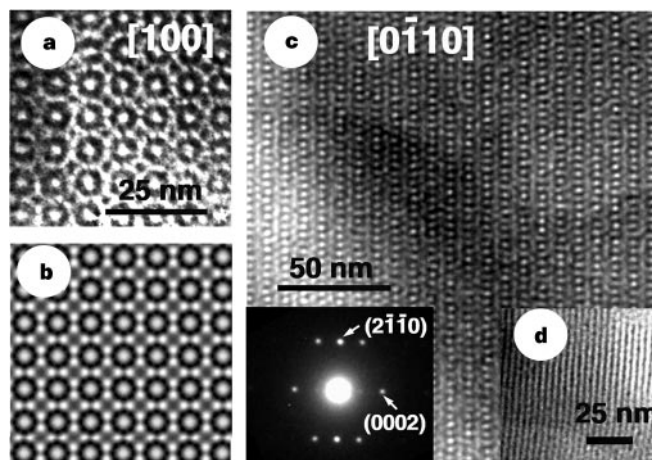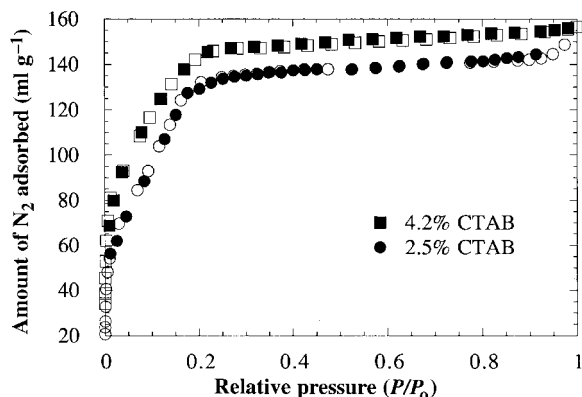
Figure 5 N_2 sorption isotherms obtained at 77 K for a 400-nm thick incipient 1-dH film prepared with $c_o = 0.06$ M (adsorption, white circles; desorption, black circles) and a 250-nm-thick cubic 3-dH film prepared with $c_0 = 0.10$ M (adsorption, white squares; desorption, black squares). The films were applied to ~1 cm^2 area of a piezoelectric ST-cut quartz substrate with interdigital gold transducers designed to operate at ~97 MHz. Mass change was monitored (~80 pg cm^{-2} sensitivity) as a function of relative pressure using a surface acoustic wave technique[21].

membrane lipid/water systems[19]. It has been suggested that two lipid bilayers transform through an inverted micellar intermediate to a cubic mesophase[20]. We propose that the 3-dH film is derived from the parent cubic film by constrained one-dimensional shrinkage during calcination[3]. The cubic → 3-dH transformation can be considered as a constrained one-dimensional distortion of the cubic cell along the [110]-direction. Comparable lattice parameters between the two mesophases allow seamless transitions between ordered domains and cause cubic and 3-dH domains to be essentially indistinguishable in plan-view (Fig. 4c).

A surface acoustic wave technique[21] was used to determine pore accessibility of supported films. Figure 5 compares nitrogen sorption isotherms of the incipient 1-dH and cubic 3-dH films. Despite the substantially different degrees of ordering, the isotherms are qualitatively similar. The lack of hysteresis and absence of any appreciable adsorption at relative pressures above 0.3 is consistent with a unimodal porosity with no interparticle meso- or macroporosity[22]. The surface areas calculated for the cubic 3-dH and incipient 1-dH films are 734 and 648 m^2 g^{-1}, respectively, demonstrating the accessibility of the mesophase porosity. In addition, the trans-film flux of cubic 3-dH films prepared as supported membranes increased by over 1,000× upon calcination, establishing through-thickness pore connectivity (A. Tsai, unpublished results).

We have demonstrated a rapid, continuous process, enabling the practical utilization of mesostructures in thin-film form. The uniform three-dimensional pore channel systems of cubic 3-dH films and the absence of granularity suggest applications in molecular separation, catalysis and sensors. The dip-coating procedure combined with the optical probe technique enables us to follow the progressive evolution of the mesostructured films and should provide insight into the synthesis of complex, self-organized organic/inorganic assemblies in general[23]. □

1. Kresge, C. T., Leonowicz, M. E., Roth, W. J., Vartuli, J. C. & Beck, J. S. Ordered mesoporous molecular sieves synthesized by a liquid-crystal template mechanism. *Nature* **359,** 710–712 (1992).
2. Beck, J. S. *et al.* A new family of mesoporous molecular sieves prepared with liquid crystal templates. *J. Am. Chem. Soc.* **114,** 10834–10843 (1992).
3. Yang, H., Kuperman, A., Coombs, N., Mamiche-Afara, S. & Ozin, G. A. Synthesis of oriented films of mesoporous silica on mica. *Nature* **379,** 703–705 (1996).
4. Yang, H., Coombs, N., Sokolov, I. & Ozin, G. A. Free-standing and oriented mesoporous silica films grown at the air–water interface. *Nature* **381,** 589–592 (1996).
5. Aksay, I. A. *et al.* Biomimetic pathways for assembling inorganic thin films. *Science* **273,** 892–898 (1996).
6. Ogawa, M. Formation of novel oriented transparent films of layered silica-surfactant nanocomposites. *J. Am. Chem. Soc.* **116,** 7941–7942 (1994).
7. Ogawa, M. A simple sol-gel route for the preparation of silica-surfactant mesostructured materials. *Chem. Commun.* 1149–1150 (1996).
8. Manne, S. & Gaub, H. E. Molecular organization of surfactants at solid–liquid interfaces. *Science* **270,** 1480–1482 (1995).
9. Brinker, C. J. *et al.* in *Access in Nanoporous Materials* (eds Pinnavaia, T. J. & Thorpe, M. F.) 123–139 (Plenum, New York, 1995).
10. Brinker, C. J. & Scherer, G. W. in *Sol–Gel Science* 120 (Academic, San Diego, 1990).
11. Brinker, C. J., Hurd, A. J., Schunk, P. R., Frye, G. C. & Ashley, C. S. Review of sol-gel thin film formation. *J. Non-Cryst. Solids* **147, 148,** 424–436 (1992).
12. Nishida, F. *et al. In situ* fluorescence probing of the chemical-changes during sol-gel thin-film formation. *J. Am. Ceram. Soc.* **78,** 1640–1648 (1995).
13. Shinitzky, M., Dianoux, A. C., Gitler, C. & Weber, G. Microviscosity and order in the hydrocarbon region of micelles and membranes determined with fluorescent probes: I, Synthetic micelles. *Biochemistry* **10,** 2106–2113 (1971).
14. Auvray, X., Petipas, C., Anthore, R., Rico, I. & Lattes, A. X-ray diffraction study of mesophases of cetyltrimethylammonium bromide in water, formamide, and glycerol. *J. Phys. Chem.* **93,** 7458–7464 (1989).
15. Ryoo, R., Kim, J. M., Ko, C. H. & Shin, C. H. Disordered molecular sieve with branched mesoporous channel network. *J. Phys. Chem.* **100,** 17718–17721 (1996).
16. Pashley, R. M. & Israelachvili, J. N. A comparison of surface forces and interfacial properties of mica in purified surfactant solutions. *Colloids Surf.* **2,** 169–187 (1981).
17. Monnier, A. *et al.* Cooperative formation of inorganic organic interfaces in the synthesis of silicate mesostructures. *Science* **261,** 1299–1303 (1993).
18. Israelachvili, J. N., Mitchell, D. J. & Ninham, B. W. Theory of self-assembly of hydrocarbon amphiphiles into micelles and bilayers. *J. Chem. Soc.* **2,** 1525–1568 (1976).
19. Lindblom, G. & Reifors, L. Cubic phases and isotropic structures formed by membrane lipid—possible biological relevance. *Biochim. Biophys. Acta* **988,** 221–256 (1989).
20. Siegel, D. Inverted micellar structures in bilayer membranes. *J. Biophys.* **45,** 399–420 (1986).
21. Frye, G. C., Ricco, A. J., Martin, S. J. & Brinker, C. J. Characterization of the surface area and porosity of sol-gel films using SAW devices. *Mat. Res. Soc. Symp. Proc.* **121,** 349–354 (1988).
22. Greg, S. J. & Sing, K. S. W. *Adsorption, Surface Area, and Porosity* 2nd edn (Academic, New York, 1982).
23. Mann, S. & Ozin, G. A. Synthesis of inorganic materials with complex form. *Nature* **382,** 313–318 (1996).

Extraction of a hydrophilic compound from water into liquid CO$_2$ using dendritic surfactants

A. I. Cooper*, **J. D. Londono**†‡, **G. Wignall**†,
J. B. McClain*, **E. T. Samulski***, **J. S. Lin**†, **A. Dobrynin***,
M. Rubinstein*, **A. L. C. Burke***, **J. M. J. Fréchet**§
& J. M. DeSimone*

* *Department of Chemistry, CB#3290, Venable and Kenan Laboratories, University of North Carolina at Chapel Hill, Chapel Hill, North Carolina 27599-3290, USA*
† *Oak Ridge National Laboratory, Oak Ridge, Tennessee 37381-6031, USA*
‡ *Department of Chemical Engineering, University of Tennessee, Knoxville, Tennessee 37996-220, USA*
§ *Department of Chemistry, University of California-Berkeley, Berkeley, California 94720, USA*

Dendrimers are well defined, highly branched polymers[1–5] that adopt a roughly spherical, globular shape in solution. Their cores are relatively loosely packed and can trap guest molecules[5–7], and by appropriate functionalization of the branch tips the macromolecules can act as unimolecular micelle-like entities[6]. Here we show that dendrimers with a fluorinated shell are soluble in liquid carbon dioxide and can transport CO$_2$-insoluble molecules into this solvent within their cores. Specifically, we demonstrate the extraction of a polar ionic dye, methyl orange, from water into CO$_2$ using these fluorinated dendrimers. This observation suggests possible uses of such macromolecules for the remediation of contaminated water, the extraction of pharmaceutical products from fermentation vessels, the selective encapsulation of drugs for targeted delivery[6,7] and the transport of reagents for chemical